ENVIRONMENTAL RESEARCH
LETTERS

LETTER • OPEN ACCESS

Physical mechanisms for the dominant summertime high-latitude atmospheric teleconnection pattern and the related Northern Eurasian climates

To cite this article: Jin-Yong Kim and Kyong-Hwan Seo 2023 *Environ. Res. Lett.* **18** 104022

ENVIRONMENTAL RESEARCH
LETTERS

LETTER

Physical mechanisms for the dominant summertime high-latitude atmospheric teleconnection pattern and the related Northern Eurasian climates

Jin-Yong Kim[1] and Kyong-Hwan Seo[1,2,3,*]

[1] Department of Atmospheric Sciences, Pusan National University, Busan, Republic of Korea
[2] Research Center for Climate Sciences, Pusan National University, Busan, Republic of Korea
[3] BK21 School of Earth and Environmental Systems, Pusan National University, Busan, Republic of Korea
* Author to whom any correspondence should be addressed.

E-mail: khseo@pusan.ac.kr

Keywords: summer atmospheric teleconnection, high latitudes, synoptic-scale eddy activity, diabatic heating, nonlinear stationary wave model

Supplementary material for this article is available online

OPEN ACCESS

RECEIVED
22 May 2023

REVISED
13 September 2023

ACCEPTED FOR PUBLICATION
15 September 2023

PUBLISHED
25 September 2023

Abstract

Summertime atmospheric teleconnection patterns over Eurasia have a significant influence on regional weather and climate. Despite extensive studies on the subtropical patterns, the high-latitude counterpart has received relatively less attention. This study proposes physical mechanisms for the formation and maintenance of the dominant high-latitude teleconnection pattern. The formation of the pattern is associated with variability in synoptic-scale eddy activity due to the meridional gradient of sea surface temperature anomalies in the vicinity of the Gulf Stream, causing a meridional shift of the central axis of storm track at the exit of Atlantic jet. The resultant convergence of transient vorticity fluxes to the west of the British Isles induces low-frequency cyclonic circulation anomalies and continued propagation of Rossby waves downstream along northern Eurasia. Once these circulation anomalies are formed, the subsequent latent heat-related diabatic anomalies over the northern Eurasian landmass act as another source of Rossby waves to maintain the teleconnection pattern. Regional temperature and precipitation variability is closely linked to the wave pattern along a route through northern Eurasia, and even precipitation over the East Asian summer monsoon region is influenced by the teleconnection pattern.

1. Introduction

In recent decades, severe heat waves, characterized by anomalous high temperatures resulting from high-pressure anomalies lasting at least two weeks in Europe or Russia, have more frequently occurred. In particular, heat waves in Eurasia occurred in the summers of 2003, 2010, and 2020 (figure 1), causing enormous socio-economic impacts and human and ecological damages in these regions. The 2003 European heat wave, the hottest summer recorded in Europe since 1540, resulted in the deaths of more than 70 000 people across Europe and damaged grain crops in southern Europe (figure 1(a)) (Robi *et al* 2008). In addition, the 2010 heat wave that affected the northern hemisphere recorded a maximum temperature of 53 °C in Eastern Europe (Ukraine, Kazakhstan, Belarus, and Georgia) and Russia, causing more than 55 000 deaths in Russia and about $500 billion in damage in northern hemisphere (figure 1(b)) (UNDRR, CRED 2020). Meanwhile, due to the Siberia heat wave that occurred in June 2020, the Arctic Circle recorded the highest temperature of 38 °C in the northeastern region of Siberia, resulting in ecosystem changes such as many wildfires, pest infestations, and melting permafrost (figure 1(c)) (Overland and Wang 2021).

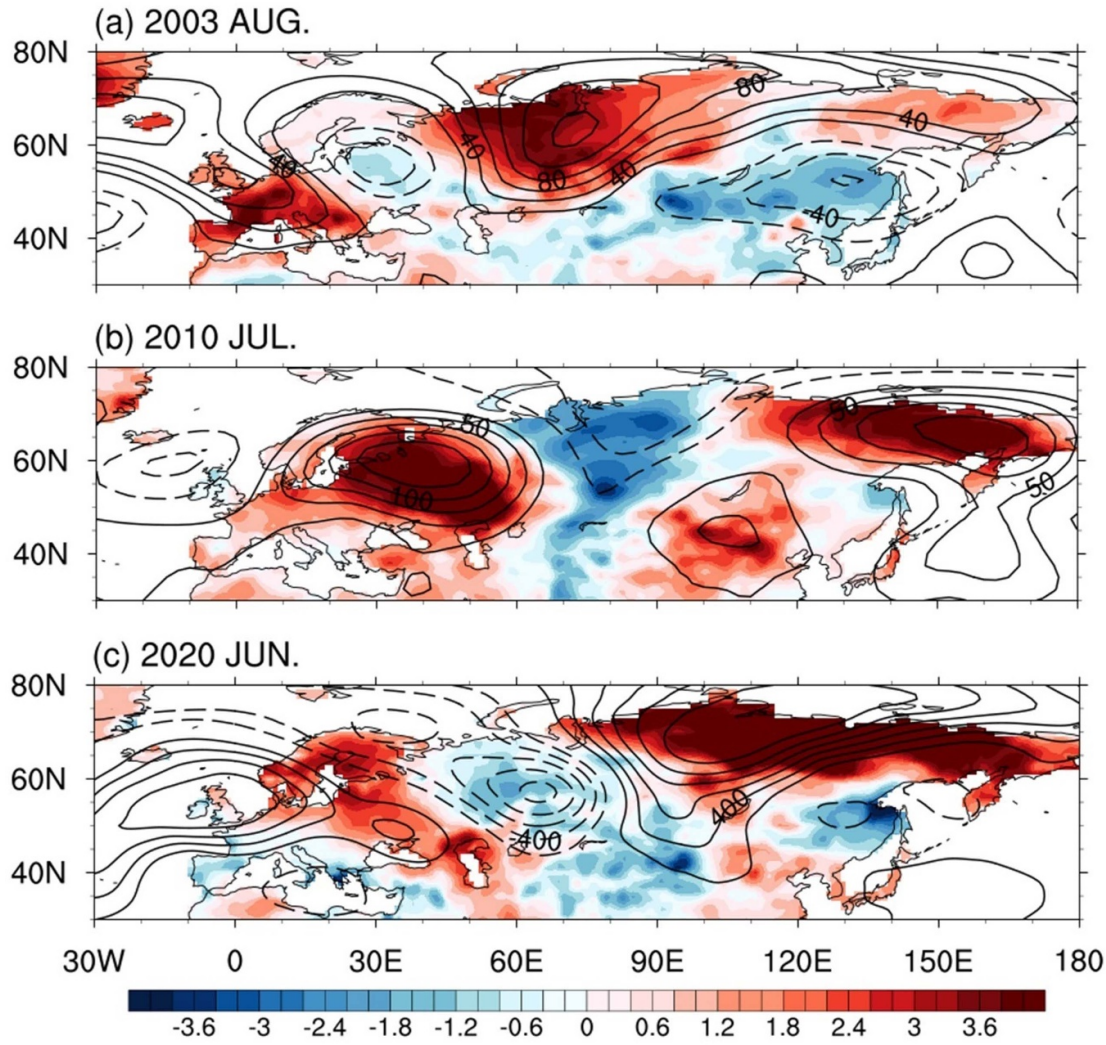

Figure 1. The monthly mean 500 hPa geopotential height (contour; gpm) and surface temperature (shading; K) anomalies in (a) August 2003 (when a heat wave event occurred over western Europe), (b) July 2010 (when a heat wave event occurred over eastern Europe and western Russia), and (c) June 2020 (when a heat wave event occurred over Siberia), respectively.

Previous studies have suggested that the well-known large-scale teleconnection patterns in summer, such as the silk road pattern (SRP) and circumglobal teleconnection along upper-atmosphere subtropical jets, may be responsible for persistent extreme weather conditions (Zhu and Li 2016, Li *et al* 2021). However, the extreme weather-related teleconnection patterns mentioned in figure 1 tend to be confined and propagate along the higher latitudes of the Eurasian continent, where the polar front jet (PFJ) is located. The summer PFJ waveguide in the higher latitudes has not been receiving much attention compared to the summer subtropical jet waveguide (Nakamura and Fukamachi 2004, Iwao and Takahashi 2008). However, the maximum variance of total wavenumber K (K_s), indicating a favorable region for propagation of barotropic quasi-stationary Rossby waves, appears to have a large value not only over the low latitude where the subtropical jet locates but also over the northern Eurasian region (figure S1 in the supporting information). This suggests two distinctive pathways for Rossby wave teleconnection on the Eurasian continent in summer. Also, several studies proposed that the meridional gradient of potential vorticity (PV) is much more important (in other words, stretching vorticity is more important) than the meridional gradient of absolute vorticity for the Rossby wave propagation over the northern Eurasian continent in summer (figure 2(b)) (Hoskins *et al* 1985, Iwao and Takahashi 2008, Wirth 2020, Woollings *et al* 2023).

Recent studies provide support for the importance of high-latitude teleconnection patterns on the northern Eurasian continent during the summer season. Xie and Kosaka (2016) analyzed the second empirical orthogonal function (EOF) mode using 300 hPa meridional wind data over this region and suggested a relationship with the development of the Okhotsk high-pressure system. However, this study did not offer insights into the formation mechanisms, nor did it provide information on the antecedent conditions that may have led to their development.

Li and Ruan (2018) proposed an Atlantic-Eurasian high-latitude teleconnection pattern with five centers of action linked to tropical and subtropical diabatic forcing through idealized model experiments. Meanwhile, Xu *et al* (2019) identified that vorticity forcing in the North Atlantic (NA) region can be the primary driver of the dominant summertime high-latitude teleconnection pattern (BBC pattern) using the reanalysis data. However, their follow-up work (Xu *et al* 2022) using the linear baroclinic model does not simulate this teleconnection pattern well, particularly in the downstream region. Furthermore, several studies (Li and Zhang 2014, Huang *et al* 2015, Wu and Francis 2019, Li *et al* 2021, Xu *et al* 2021, Liu *et al* 2022, 2023) have demonstrated that summertime high-latitude teleconnection patterns associated with PFJs can exert a significant influence on the variability of northern Eurasian and East Asian climates.

Despite the recent advances in identifying high-latitude teleconnection patterns, a comprehensive understanding of the precise mechanisms governing the formation and maintenance of the patterns is still lacking. In this study, our primary goal is to demonstrate the detailed physical mechanisms, with a causal relationship focus, governing the formation and maintenance of the dominant summertime high-latitude atmospheric teleconnection pattern. To support our findings, we employ a nonlinear stationary model (SWM) and quantitatively identify the potential for high-latitude Rossby wave propagation through a ray tracing technique. In addition, we illustrate how this pattern relates the climate of both the northern Eurasian region and the East Asian region. These approaches will contribute to better our understanding of the summertime high-latitude teleconnection pattern over the northern Eurasian continent.

2. Data and methods

The data used includes the following: (1) The monthly mean atmospheric reanalysis data with a horizontal resolution of 1.25° × 1.25° from Japanese 55 year Reanalysis (JRA-55) data provided by the Japanese Meteorological Agency (Kobayashi *et al* 2015). (2) The monthly precipitation data from the Global Precipitation Climatology Project (GPCP) version 2.3 dataset provided by NOAA/OAR/ESRL PSD with 2.5° × 2.5° latitude-longitude resolution (Adler *et al* 2003). Only boreal summer, from June to August (JJA), is considered for the period of 1979–2019.

An EOF analysis is employed to extract the dominant atmospheric teleconnection mode on the northern Eurasian continent. In order to understand the associated spatial patterns, a composite analysis is conducted using the obtained EOF principal component (PC) time series. A 2–6 day Lanczos bandpass filter is applied to obtain signals associated with synoptic-scale disturbances (Duchon 1979). The three-dimensional (3D) wave activity flux (WAF) is calculated to represent the propagation of Rossby wave packets (Takaya and Nakamura 2001). Also, to identify the evolution of wave activity, a ray tracing analysis is performed to the horizontally nonuniform flow by using the divergent barotropic Rossby wave theory (Hoskins and Karoly 1981, Hoskins and Ambrizzi 1993). The ray path of the Rossby wave activity, which is determined by group velocity (c_{gx} and c_{gy}), is computed by using a fourth-order Runge–Kutta method (Press *et al* 2007, Seo *et al* 2012, 2016, 2017):

$$\omega = \bar{u}_M k + \bar{v}_M l + \frac{\bar{q}_x l - \bar{q}_y k}{K^2}, \tag{1}$$

$$\frac{\mathrm{d}x}{\mathrm{d}t} = c_{gx} = \bar{u}_M + \frac{\left(k^2 - l^2\right)\bar{q}_y - 2kl\bar{q}_x}{K^4}, \tag{2}$$

$$\frac{\mathrm{d}y}{\mathrm{d}t} = c_{gy} = \bar{v}_M + \frac{\left(k^2 - l^2\right)\bar{q}_x - 2kl\bar{q}_y}{K^4}, \tag{3}$$

where ω is frequency ($\omega = 0$, for stationary Rossby wave), $\bar{u}_M$ and $\bar{v}_M$ represent the basic zonal and meridional flow on a Mercator projection, $K^2 = \sqrt{k^2 + l^2 + \frac{1}{L_R^2}}$ (the total wavenumber), with k and l being zonal and meridional wavenumbers, $L_R \equiv \frac{(gH)^{1/2}}{f_0}$ (the Rossby radius of deformation), with g, H and f_0 being the gravitational acceleration, scale height, and Coriolis parameter, respectively. The zonal and meridional gradients of quasi-geostrophic PV $\bar{q}_x$ and $\bar{q}_y$ take the form $\bar{q}_x = \frac{1}{a^2\cos\varphi}\left(\frac{\partial^2\bar{v}}{\partial\lambda^2} - \frac{\partial^2\bar{u}}{\partial\varphi\partial\lambda}\cos\varphi + \frac{\partial\bar{u}}{\partial\lambda}\sin\varphi\right) - \frac{\bar{v}}{\cos\varphi L_R^2}$ and $\bar{q}_y = \frac{\partial f}{\partial y} - \frac{\partial^2\bar{u}_M}{\partial y^2} + \frac{\partial^2\bar{v}}{a^2\partial\varphi\partial\lambda} + \tan\varphi\frac{\partial\bar{v}}{a^2\partial\lambda} + \frac{\bar{u}}{\cos\varphi L_R^2}$.

To simulate the atmospheric teleconnection pattern and examine the dominant forcing mechanism of stationary Rossby waves, we use a SWM (Ting and Yu 1998). This SWM is a fully nonlinear baroclinic model with a dry dynamical core. For damping, Rayleigh friction and Newtonian cooling terms are included in the momentum and temperature equations. In this study, we use rhomboidal truncation at wavenumber 15 in the horizontal space (R30) with 24 vertical sigma (σ) levels. For further details of the model, see Ting and Yu (1998) and Simpson *et al* (2016).

3. Results

3.1. Dominant summertime teleconnection pattern in northern Eurasian continent

Previous observational analysis demonstrated several recurring and persistent patterns that can explain a considerable portion of the Northern Hemisphere low-frequency variability using statistical methods such as the temporal correlation approach, PC analysis (PCA), rotated PCA, and cluster analysis (Horel 1981, Wallace and Gutzler 1981, Barnston and Livezey 1987, Johnson *et al* 2008). In this study, to extract

the leading atmospheric teleconnection pattern in the NH mid-high latitudes, EOF analysis is applied to 250 hPa meridional wind anomalies over the region of 50 °W–150 °E, 50 °–80 °N. The selected region corresponds to the largest interannual variability of 250 hPa meridional winds at mid-high latitudes from the NA to the Eurasian continent (figure 2(a)). Using meridional wind anomalies for EOF to capture the wave patterns that have a shorter zonal scale is commonly used in previous studies (Xie and Kosaka 2016, Xu *et al* 2019, Li *et al* 2020).

Figure 2(c) shows the spatial pattern and temporal variation of the first EOF mode and this explains approximately 25% of the total interannual variability of atmospheric teleconnection patterns in the northern Eurasian continent during boreal summer. Based on the rule of thumb of North *et al* (1982), the first leading mode (EOF1) is well separated from other modes. The EOF1 shows four centers of action located in the eastern NA Ocean, Scandinavia, the Ural Mountains, and Lake Baikal. The positive EOF1 is indicative of cyclonic circulation anomalies at 250 hPa over the eastern NA Ocean and Ural Mountains, and anticyclonic circulation anomalies over Scandinavia and Lake Baikal (figure 2(d)).

To compare with the previously well-known atmospheric teleconnection patterns, we calculated the correlation coefficient for each pattern. As a result, the EOF1 time series shows a statistically significant relationship with the East Atlantic/West Russia (EA/WR) index ($r = 0.56$) at 99% confidence level, but when we see the details of its pressure anomaly pattern, some marked differences exist. In particular, over the NA region, EOF1 shows a NE [30°–10 °W, 45°–75 °N]–SW [70°–50 °W, 35–45 °N] tilted dipole pattern, but EA/WR shows a horizontally elongated pattern (figure S2). Also, teleconnection pattern in the subtropics is not well separated for EA/WR pattern. This can make it difficult to accurately identify the mid-high latitude teleconnection pattern as its signals may overlap and interact with each other in complex ways. Therefore, to understand the characteristics of a mid- and high-latitude propagating teleconnection pattern that is independent of the subtropics, the EOF1 pattern is analyzed in this study. Note that since this dominant teleconnection pattern is highly correlated with the BBC pattern identified by Xu *et al* (2019), this mode is hereafter referred to as the BBC pattern.

When we see the vertical profile of the BBC pattern related to its center of action, it clearly shows the westward tilted equivalent-barotropic structure (figure 2(e)) in the lower-mid troposphere. This vertically tilted structure is associated with the baroclinic energy conversion that takes place through the eddy heat flux across the climatological temperature gradient, transferring available potential energy from the background field to the eddy field. The maximum values of omega are located in between the pressure centers, facilitating poleward transport of energy. The WAF plot provides insights into the origin and dissipation of waves, facilitating comprehension of the mechanics underlying the behavior of the large-scale Rossby wave. It is notable that low-level WAF over the NA region [60°–10°W] in BBC pattern shows the vertically propagating pattern, implying the possible source region of forcing (figure 2(e)).

3.2. Possible formation mechanisms and its impact on climate in northern Eurasia

Previous studies have suggested a link between teleconnection patterns propagating across the Eurasian continent and sea surface temperature anomalies (SSTAs) in the NA (Wu *et al* 2009, Sun *et al* 2015, Li and Ruan 2018). Figure 3(a) shows the tripolar SSTAs, with particularly strong negative anomalies to the west of the British Isles, yet the associated diabatic heating and cooling response in the tropical or subtropical regions is weak or insignificant.

On the other hand, cold SSTAs around 40°–60 °N and warm anomalies around 35 °N tend to strengthen the meridional gradient of SST around 40 °N (figures 3(a) and (b)). This SSTAs pattern may serve to continuously support the mid-latitude synoptic eddies (figure 3(c)), which play a significant role in the formation of the BBC-related teleconnection pattern. Figure 3(c) shows 700 hPa maximum Eady growth rate (EGR) related to the BBC pattern. The EGR is given by $0.3098\left(\frac{f}{N}\right)|\partial U(z)/\partial z|$, where f is the Coriolis parameter, N the static stability, and U the zonal wind. The increase in synoptic eddy activity due to the low level baroclinicity associated with the positive EGR anomaly near the Gulf stream (70°–20 °W, 40°–50 °N) can shift the central axis of the storm track south–eastward (20°–5 °W, 40°–50 °N) compared to the climatological location (figure 3(d), shading). This direction of wave energy propagation is demonstrated by Hoskins *et al* (1983) based on observational analysis using extended Eliassen-Palm vectors. In short, the synoptic eddies originate from low levels at the entrance of the storm track, propagate eastward along the central axis of the storm track, and then propagate equatorward at its end.

The convergence of transient vorticity flux has a strong tendency to occur on the leftward side of the central axis of the storm track (Jin *et al* 2006a, 2006b, Kug and Jin 2009) and anomalous low-frequency circulation can be enhanced by eddy vorticity fluxes (Hoskins *et al* 1983, Lau and Holopainen 1984, Lau 1988). The following equation represents the relationship between the geopotential height tendency and the vorticity fluxes of high-frequency transient eddies:

$$\frac{\partial Z'}{\partial t} = \frac{f}{g}\nabla^{-2}\left(-\nabla\cdot\overline{V'\varsigma'}\right), \tag{4}$$

where f indicates the Coriolis parameter, g is the gravitational acceleration, V is the horizontal wind, ζ is

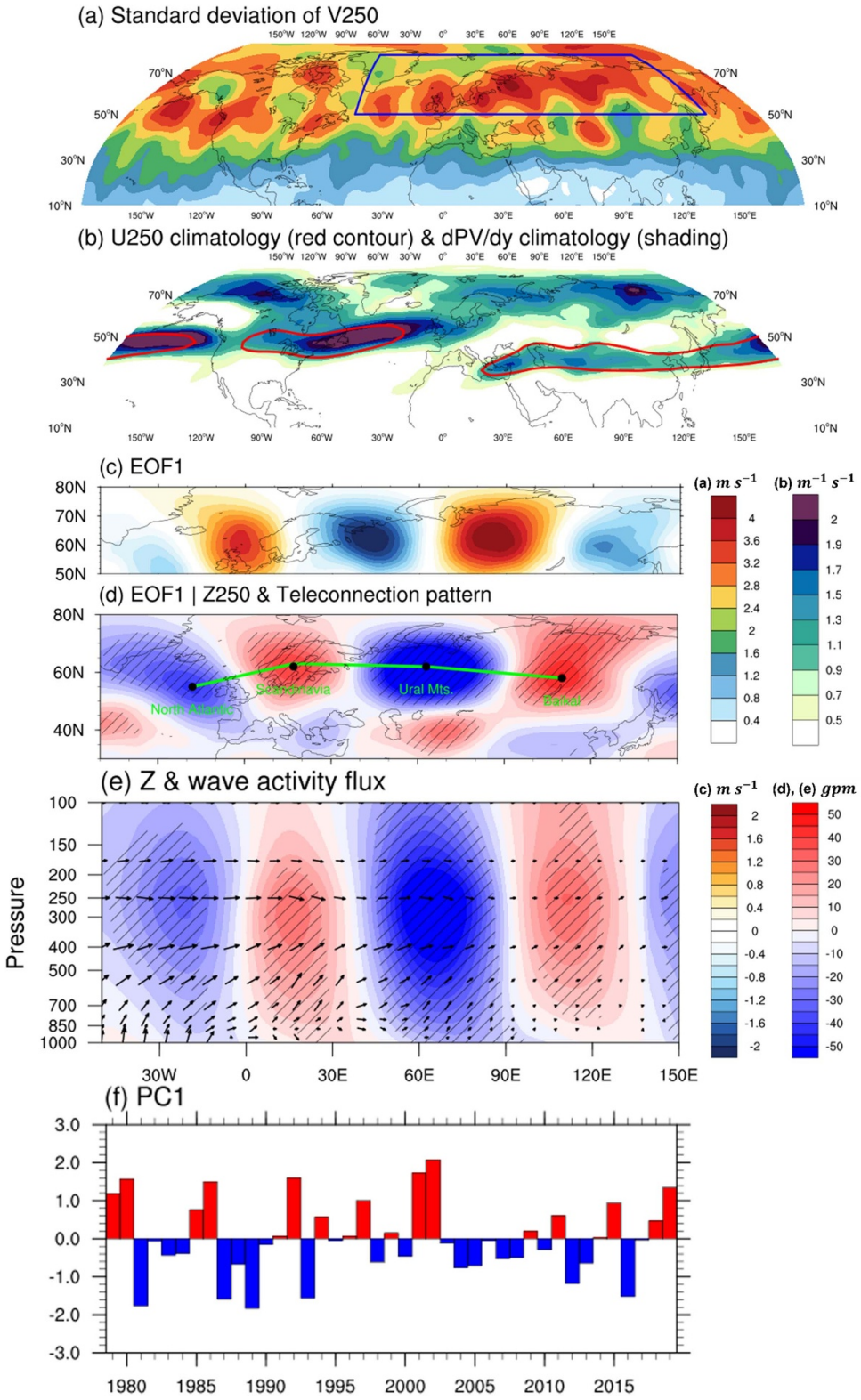

Figure 2. (a) The standard deviation of the summertime (June–July–August) climatological 250 hPa meridional winds (shading; $m^2\ s^{-2}$) during the period of 1981–2010. The blue box indicates the region of EOF analysis. (b) The meridional gradient of the climatological summer mean 250 hPa PV (shading; $m^{-1}\ s^{-1}$). The red contours indicate the 20 m s^{-1} contour of climatological 250 hPa summer mean zonal wind. (c) Spatial patterns of the leading EOF mode of summertime 250 hPa meridional wind anomaly (shading; m s^{-1}) in mid-high latitude. Composite difference (strong minus weak) maps of (d) 250 hPa geopotential height anomaly (shading; gpm) from JJA using the PC1 time series for 1979–2019 and teleconnection pattern along the solid green line. (e) The vertical cross section of composite difference geopotential height anomaly (shading; gpm) and wave activity flux (vector; $m^2\ s^{-2}$). (f) The corresponding normalized PC time series. Composite criteria are ±0.75. Hatching indicates the 95% confidence levels based on the two-tailed Student's *t* test. Ten positive years: 1979, 1980, 1985, 1987, 1992, 1997, 2001, 2002, 2015, and 2019; and seven negative years: 1981, 1987, 1989, 1993, 2004, 2012, and 2016.

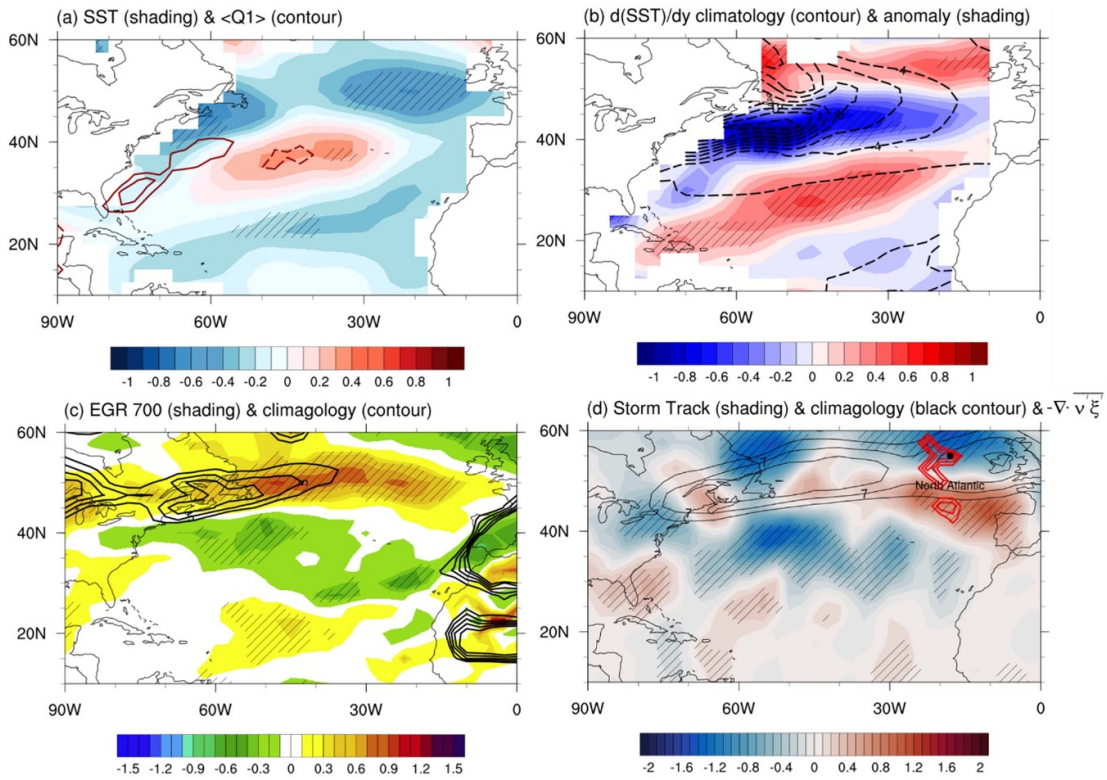

Figure 3. Composite difference maps of (a) sea surface temperature anomalies (shading; K) and vertically integrated diabatic heating ($Q1 = \frac{\partial T}{\partial t} - V \cdot \nabla T - \sigma\omega$; red contour; 95% confidence level), where T is the air temperature, V the horizontal wind, σ the static stability, and ω the vertical velocity, (b) meridional gradient of SSTAs (shading; 10^6 K) and its climatology (black contour; 10^6 K), (c) 700 hPa Eady growth rate (shading; s^{-1}) anomalies and its climatology (black contour; s^{-1}), (d) storm track(shading; $m^2\ s^{-2}$) anomalies, storm track climatology (black contour; $m^2\ s^{-2}$), and convergence of transient vorticity flux anomalies (red contour, 95% confidence level). Negative contours are dashed and hatching indicates the 95% confidence levels based on the two-tailed Student's t test.

the relative vorticity, ∇ is the horizontal gradient, the overbar denotes the time average, and the prime represents the high frequency quantities. Since inverse Laplacian qualitatively indicates minus sign, a negative (positive) geopotential height anomaly appears in the region where transient vorticity flux converges (diverges). In other words, enhanced eddy activity associated with the strengthening of the meridional gradient of SSTAs in the vicinity of the Gulf Stream could cause a low-frequency cyclonic circulation anomaly in the upper-troposphere to the west of the British Isles (as shown in figure 2(d)). Furthermore, high-frequency transient vorticity fluxes can act as the Rossby wave source at the exit of the Atlantic jet, causing propagation of anomalous stationary Rossby wave downstream (Teng *et al* 2013, Schubert *et al* 2014, Teng and Branstator 2019). The geopotential height anomalies associated with transient vorticity fluxes in northern Eurasia, as depicted in figure 4(a), illustrates the significance of high-frequency transient feedback in developing and maintaining the leading EOF mode-related upper atmospheric pattern (Schubert *et al* 2011, Teng *et al* 2019, Xu *et al* 2019).

The nonlinear SWM is used to clarify the mechanisms underlying the formation and maintenance of stationary wave teleconnection through transient vorticity fluxes (Ting and Yu 1998, Simpson *et al* 2016). The idealized anomaly for the convergence of transient vorticity flux [46°–60°N, 335°–342°E] over the NA is forced. The horizontal and vertical profile of the prescribed forcing are shown in figures 5(a) and (d). The simulated response closely resembles the observed geopotential anomalies in the upper troposphere, exhibiting a pattern correlation of approximately 0.61 (figures 2(d) and 5(a)). However, the simulated cyclonic (anticyclonic) circulation anomaly over the Ural Mountains (Scandinavia and Lake Baikal) displays a slightly different center of action and a rather smaller amplitude compared to the observed anomaly. These discrepancies in the simulated anomalous stationary waves may be attributed to factors such as an inaccurate dissipation parameterization or other unaccounted physical phenomena (Liu *et al* 1998, Ting *et al* 2001, Sobolowski *et al* 2011, Behera *et al* 2013). Nevertheless, there exists a strong concurrence among the ray path of Rossby wave activity (depicted by the blue line in figure 5(a)), the center of action response of the model simulation (figure 5(a)), and the large meridional gradient of PV area (figure 2(b)). However, even though the above eddy vorticity forcing is the primary driver for the downstream wave propagation, this does not produce

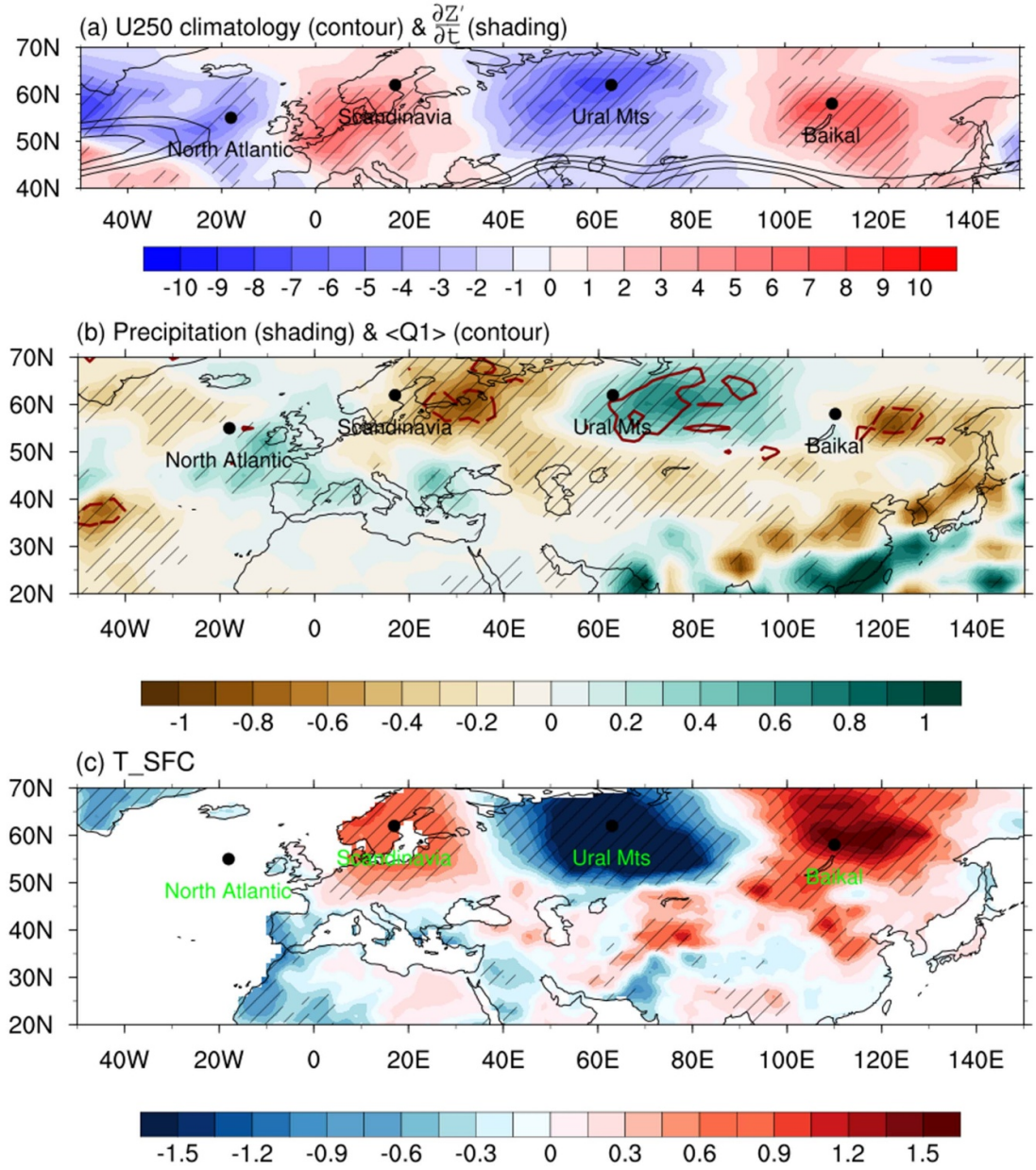

Figure 4. Composite difference maps of (a) geopotential height tendency induced by high-frequency transient eddies (shading; gpm day^{-1}), and climatological 250 hPa summer mean zonal wind (black contour; m s^{-1}), (b) Precipitation anomalies (shading; mm day^{-1}) and vertically integrated diabatic heating (red contour; 95% confidence level), and (c) surface temperature anomalies (shading: K) from JJA using the PC1 time series for 1979–2019. Negative contours are dashed and hatching indicates the 90% confidence levels based on the two-tailed Student's *t* test.

large enough anomalies shown in the observation—in particular, those over the Ural Mountains and Lake Baikal.

The anomalous Rossby wave propagating through northern Eurasia in the summertime basic state (figure S3, i.e. land–sea thermal contrast and lower stability in the midtroposphere) could be maintained for a longer period (Xu *et al* 2019, 2020, Li *et al* 2020). The Rossby waves from the NA towards the Eurasian continent can induce atmospheric disturbances that cause changes in temperature, moisture, and pressure. These changes can then lead to the generation of diabatic heating or cooling and this can act as a source of Rossby wave and influence the maintenance of the teleconnection pattern. The diabatic heating (cooling) anomalies associated with precipitation or temperature advection anomalies of the BBC pattern coincide with the center of the omega in the mid-troposphere and are located about a 1/4 wavelength east of the center of the geopotential height anomalies (figure 4(b)). To examine the effect of diabatic forcing, we considered three areas over the continent [25°–47.5 °E, 55°–70 °N; 62.5°–95 °E, 52.5°–67.5 °E; 117.5°–135 °E, 50°–57.5 °N] with statistically significant diabatic forcing in relation to the observed precipitation anomalies (as shown in figure 4(b)). Detailed information about the experimental setting is presented in figure 5. Figure 5(b) shows the

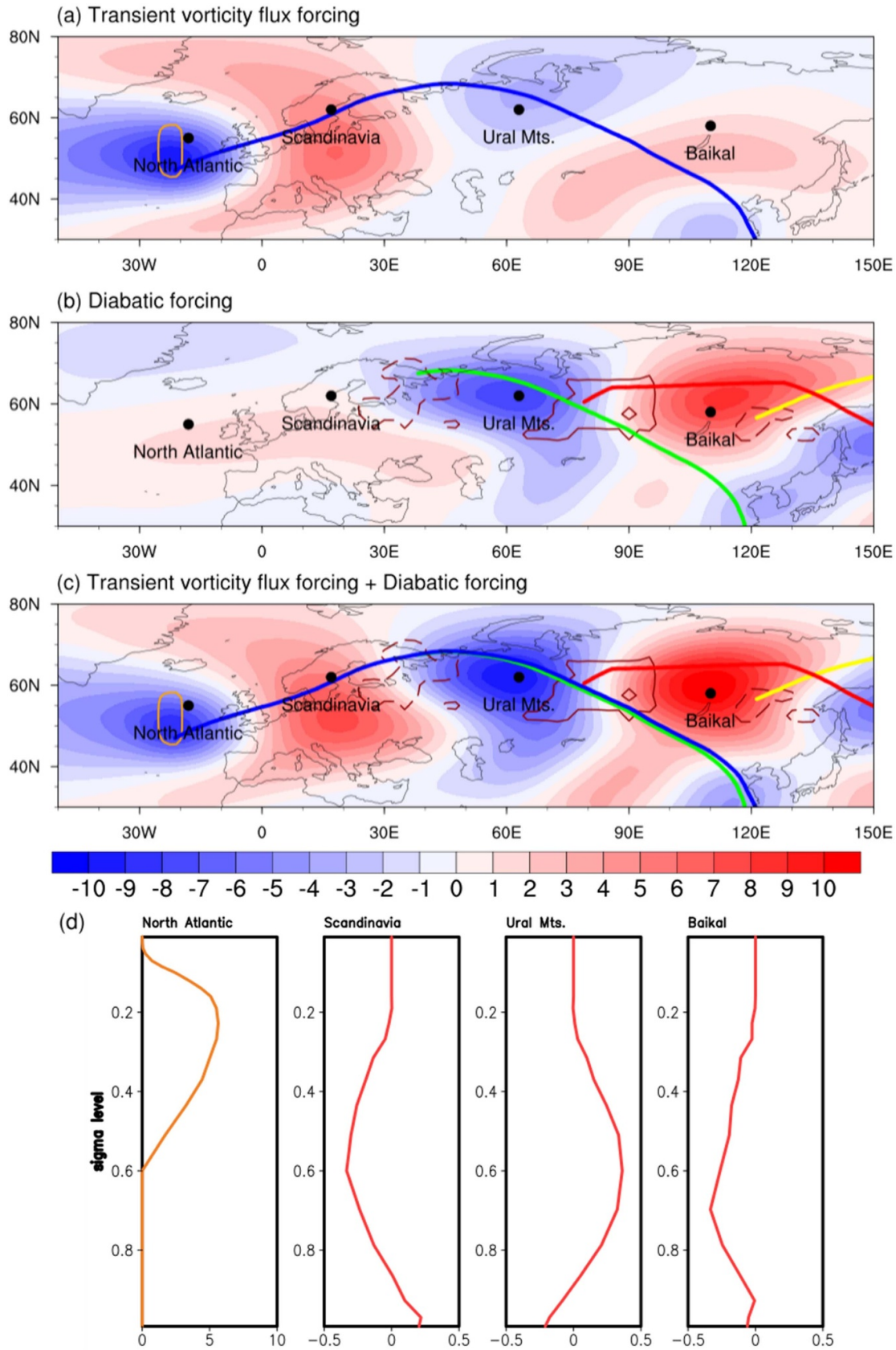

Figure 5. The teleconnection pattern in the 250 hPa geopotential height anomalies (shading; gpm) from nonlinear stationary wave model simulations forced by (a) the idealized transient vorticity forcing (orange contour is at $\sigma = 0.27$ (3×10^{-11} s^{-2}), (b) the diabatic forcing (red contour is denoted at $\sigma = 0.44$ (10^{-6} K s^{-1}), and (c) the transient vorticity forcing + the vertically integrated diabatic forcings. Blue, green, red, and yellow lines denote the Rossby wave ray path for waves with the zonal wavenumber 3. (d) The vertical profile at the forcing center (vorticity; 10^{-11} s^{-2}) and the area-averaged vertical profiles (diabatic heating or cooling; 10^{-5} K s^{-1}) of stationary forcing prescribed to the nonlinear stationary wave model. The basic state is the summer mean climatology during 1979–2019 based on JRA-55 datasets.

simulated response to vertically integrated diabatic heating (cooling) forcing over the northern Eurasian continent, demonstrating a strong pattern correlation with the observed spatial pattern of the BBC ($r = 0.78$). Notably, this agreement is especially well represented over the Ural Mountains (cyclonic circulation anomaly) and Lake Baikal regions (anticyclonic circulation anomaly). The combined forcing simulation (transient vorticity flux forcing + diabatic forcing) of the nonlinear SWM exhibits the outstanding pattern correlation with the observed spatial pattern of the BBC (figure 5(c), $r = 0.90$). Results based on the observational analysis, model experiment, and theoretical approach all support the formation and maintenance mechanisms of high-latitude teleconnection patterns over the Eurasian continent.

Stationary waves can significantly shape the distributions of surface temperatures and moisture along the path of wave propagation and impact the trajectories of mid-latitude cyclones (Simpson *et al* 2016). Figures 4(b) and (c) show the composite difference map of precipitation anomaly and surface temperature (T_SFC) anomaly over the Eurasian continent during summertime related to the PC1. Along each center of high (low) pressure anomalies, positive (negative) temperature anomalies appear, and the precipitation region coincides with the location of maximum omega velocity in relation to the vertically westward tilted structure in the lower and middle troposphere over northern Eurasia. When the teleconnection pattern is positive, significant high T_SFC anomalies are observed in the Scandinavia, northeastern Russia, and Mongolia-north China; and low T_SFC anomalies are present over the western Russia (figure 4(c)). The teleconnection pattern accounts for 24%, 71%, 52%, and 24% of the total variance of areal average temperature variability over the Scandinavia, western Russia, northeastern Russia, and Mongolia-north China, respectively. Meanwhile, more precipitation occurs over northern Siberia and less over western and eastern Russia (figure 4(b)). In addition, negative precipitation anomalies appear over mid China and the Korean Peninsula, and positive precipitation anomalies appear over southern China and to the south of Korea. The teleconnection pattern accounts for 53%, 58%, 34%, 12% and 14% of the total variance of areal averaged precipitation variability over western Russia, northern Siberia, eastern Russia, mid China and the Korean peninsula, and south China and to the south of Korea, respectively. All values show statistically significant correlations at the 95% confidence level. These results suggest that the dominant teleconnection pattern in northern Eurasia has a strong connection with regional climate variability and can even affect precipitation in East Asia.

4. Conclusion and discussion

EOF analysis applied to summer 250 hPa meridional wind anomalies over the region of 50 °W–150 °E, 50°–80 °N. The leading mode (BBC pattern) shows the zonally oriented and meridionally confined teleconnection pattern and consists of several geographically fixed centers along the upper-tropospheric PFJ from the eastern NA to northern Eurasia (figures 2(b), (d) and (e)).

We demonstrate that synoptic-scale eddy activity in the vicinity of the Gulf Stream associated with the meridional gradient of SSTAs plays a more decisive role in the formation of Rossby wave propagation originating from the NA than diabatic forcing in the tropical or subtropical regions does. The increase in eddy activity causes an eastward extension and southward shift of the central axis of the Atlantic storm track, generating the convergence of transient vorticity flux on the left side of the central axis (i.e. the west of the British Isles). This convergence can generate a low-frequency cyclonic circulation anomaly over the NA and can induce the propagation of the Rossby wave along northern Eurasia. The diabatic forcing in the northern Eurasia continent induced by the upstream transient vorticity flux forcing acts as another source of Rossby waves and plays a critical role in sustaining and generating the teleconnection pattern downstream regions. Our results have been supported by the stationary wave ray tracing method applied to horizontally nonuniform horizontal flow, WAF, and simulations using a nonlinear SWM.

The BBC pattern is significantly linked to the regional climate variations in northern Eurasia and East Asia. In the positive phase of the BBC pattern in summer, higher temperatures develop in Scandinavia and Lake Baikal, and lower temperatures in the Ural Mountains. The precipitation anomalies appear around a quarter of a wavelength downstream from the center of the temperature change. Meanwhile, negative precipitation anomaly occurs over mid-north China and the Korean peninsula and positive precipitation anomaly develops over south China and to the south of Korea.

This study allows the better understanding of northern Eurasian atmospheric teleconnection patterns and helps improve the northern Eurasian continent seasonal prediction skills in summer. The complex nature of the physical, dynamical, and nonlinear processes involved in the formation and maintenance mechanisms of atmospheric teleconnection patterns over the mid-high latitudes makes it difficult to clearly understand this phenomenon. Our model results show that diabatic heating or cooling tends to induce or intensify the circulation anomaly

downstream (figure 5(b)). Our analysis and approach is similar to the well-known previous studies by Hoskins and Karoly (1981), Hoskins and Ambrizzi (1993), Wirth (2020), and Woolings *et al* (2023), where diabatic heating plays a forcing role in producing the mid- to high-latitude circulation response. However, more in-depth study will be needed to understand the role of diabatic forcing at high latitudes in summer.

Additionally, the effects of global warming and climate change further complicate the examination of these mechanisms. There are several studies pointing out that wavier circulation anomaly pattern over mid- and high-latitude regions in summer is due to the Arctic amplification (AA) related to global warming (Petoukhov *et al* 2013a, Coumou *et al* 2014, 2018, Screen and Simmonds 2014). Moreover, due to climate change, the rate of increase in the surface temperature of the northern Eurasian continent in summer is higher than that of the Arctic, so it is expected that the Arctic PFJ is strengthened, and the storm track is extended eastward, increasing the possibility of enhancing the present EOF1 mode. These changes are closely related to the recent sustained heat waves and cold waves across Europe and Russia (Day and Hodges 2018, Rousi *et al* 2022). Understanding the implications of these changes on the characteristics of high-latitude teleconnection in future climates requires further investigation.

Data availability statement

JMA provides JRA-55 data (www.jma.go.jp/jma/indexe.html). NOAA provides ERSSTv5 SST data (https://psl.noaa.gov/data/gridded/data.noaa.ersst.v5.html), and GPCPv2.3 data (https://psl.noaa.gov/data/gridded/data.gpcp.html).

Acknowledgments

The authors appreciate three anonymous reviewers for their helpful comments, which improved the manuscript. This work is supported by a National Research Foundation of Korea (NRF) grant funded by the Korean government (MSIP) (No. NRF-2020R1A2C2009414) and the Korea Meteorological Administration (KMA) Research and Development Program under Grant KMI2021–01410.

Conflict of interest

All authors declare that they have no competing interests.

ORCID iDs

Jin-Yong Kim https://orcid.org/0009-0001-6710-8855
Kyong-Hwan Seo https://orcid.org/0000-0001-6305-5488

References

Adler R F *et al* 2003 The version 2 global precipitation climatology project (GPCP) monthly precipitation analysis (1979-present) *J. Hydrometeorol.* **4** 1147–67
Barnston A G and Livezey R E 1987 Classification, seasonality, and persistence of low-frequency atmospheric circulation patterns *Mon. Weather Rev.* **115** 1083–126
Behera S, Ratnam J V, Masumoto Y and Yamagata T 2013 Origin of extreme summers in Europe: the Indo-Pacific connection *Clim. Dyn.* **41** 663–76
Coumou D, Di Capua G, Vavrus S, Wang L and Wang S 2018 The influence of Arctic amplification on mid-latitude summer circulation *Nat. Commun.* **9** 2959
Coumou D, Petoukhov V, Rahmstorf S, Petri S and Schellnhuber H J 2014 Quasi-resonant circulation regimes and hemispheric synchronization of extreme weather in boreal summer *Proc. Natl Acad. Sci.* **111** 12331–6
Day J J and Hodges K I 2018 Growing land-sea temperature contrast and the intensification of Arctic cyclones *Geophys. Res. Lett.* **45** 3673–81
Duchon C E 1979 Lanczos filtering in one and two dimensions *J. Appl. Meteorol.* **18** 1016–22
Horel J D 1981 A rotated principal component analysis of the interannual variability of the Northern Hemisphere 500 Mb height field *Mon. Weather Rev.* **109** 2080–92
Hoskins B J and Ambrizzi T 1993 Rossby wave propagation on a realistic longitudinally varying flow *J. Atmos. Sci.* **50** 1661–71
Hoskins B J, James I N and White G H 1983 The shape, propagation and mean-flow interaction of large-scale weather systems *J. Atmos. Sci.* **40** 1595–612
Hoskins B J and Karoly D J 1981 The steady linear response of a spherical atmosphere to thermal and orographic forcing *J. Atmos. Sci.* **38** 1179–96
Hoskins B J, McIntyre M E and Robertson A W 1985 On the use and significance of isentropic potential vorticity maps *Q. J. R. Meteorol. Soc.* **111** 877–946
Huang D Q, Zhu J, Zhang Y C, Wang J and Kuang X Y 2015 The impact of the East Asian subtropical jet and polar front jet on the frequency of spring persistent rainfall over southern China in 1997–2011 *J. Clim.* **28** 6054–66
Iwao K and Takahashi M 2008 A precipitation seesaw mode between Northeast Asia and Siberia in summer caused by Rossby waves over the Eurasian continent *J. Clim.* **21** 2401–19
Jin F-F, Pan L-L and Watanabe M 2006a Dynamics of synoptic eddy and low-frequency flow interaction. Part I: a linear closure *J. Atmos. Sci.* **63** 1677–94
Jin F-F, Pan L-L and Watanabe M 2006b Dynamics of synoptic eddy and low-frequency flow interaction. Part II: a theory for low-frequency modes *J. Atmos. Sci.* **63** 1695–708
Johnson N C, Feldstein S B and Tremblay B 2008 The continuum of northern hemisphere teleconnection patterns and a description of the NAO shift with the use of self-organizing maps *J. Clim.* **21** 6354–71
Kobayashi S *et al* 2015 The JRA-55 reanalysis: general specifications and basic characteristics *J. Meteorol. Soc. Jpn.* **93** 5–48

Kug J S and Jin F-F 2009 Left−hand rule for synoptic eddy feedback on low−frequency flow *Geophys. Res. Lett.* **36** L05709

Lau N-C 1988 Variability of the observed midlatitude storm tracks in relation to low-frequency changes in the circulation pattern *J. Atmos. Sci.* **45** 2718–43

Lau N-C and Holopainen E O 1984 Transient eddy forcing of the time-mean flow as identified by geopotential tendencies *J. Atmos. Sci.* **41** 313–28

Li J P and Ruan C Q 2018 The North Atlantic–Eurasian teleconnection in summer and its effects on Eurasian climates *Environ. Res. Lett.* **13** 024007

Li L and Zhang Y 2014 Effects of different configurations of the East Asian subtropical and polar front jets on precipitation during the Mei-Yu season *J. Clim.* **27** 6660–72

Li X, Lu R and Ahn J B 2021 Combined effects of the British–Baikal corridor pattern and the silk road pattern on Eurasian surface air temperatures in summer *J. Clim.* **34** 3707–20

Li X, Lu R, Greatbatch R J, Li G and Hong X 2020 Maintenance mechanism for the teleconnection pattern over the high latitudes of the Eurasian continent in summer *J. Clim.* **33** 1017–30

Liu A Z, Ting M and Wang H 1998 Maintenance of circulation anomalies during the 1988 drought and 1993 floods over the United States *J. Atmos. Sci.* **55** 2810–32

Liu L, Wu B and Ding S 2022 On the association of the summertime shortwave cloud radiative effect in Northern Russia with atmospheric circulation and climate Over East Asia *Geophys. Res. Lett.* **49** 2

Liu L, Wu B and Ding S 2023 Combined impact of summer NAO and northern Russian shortwave cloud radiative effect on Eurasian atmospheric circulation *Environ. Res. Lett.* **49** 014015

Nakamura H and Fukamachi T 2004 Evolution and dynamics of summertime blocking over the Far East and the associated surface Okhotsk high *Q. J. R. Meteorol. Soc.* **130** 1213–33

North G R, Bell T L, Cahalan R F and Moeng F J 1982 Sampling errors in the estimation of empirical orthogonal functions *Mon. Wea. Rev.* **110** 699–706

Overland J E and Wang M 2021 The 2021 Siberian heat wave *Int. J. Climatol.* **41** E2341–6

Petoukhov V, Rahmstorf S, Petri S and Schellnhuber H J 2013a Quasiresonant amplification of planetary waves and recent Northern Hemisphere weather extremes *Proc. Natl Acad. Sci.* **110** 5336–41

Press W H, Teukolsky S A, Vetterling W T and Flannery B P 2007 Numerical recipes *Art of Scientific Computing* 3rd edn (Cambridge University Press)

Robine J-M, Cheung S L K, Le R S, Van Oyen H, Griffiths C, Michel J-P and Herrmann F R 2008 Solongo *C. R. Biol.* **331** 171–8

Rousi E, Kornhuber K, Beobide-Arsuaga G, Luo F and Coumou D 2022 Accelerated western European heatwave trends linked to more-persistent double jets over Eurasia *Nat. Commun.* **13** 3851

Schubert S D, Wang H, Koster R D, Suarez M J and Groisman P Ya 2014 Northern Eurasian heat waves and droughts *J. Clim.* **27** 3169–207

Schubert S, Wang H and Suarez M 2011 Warm season subseasonal variability and climate extremes in the Northern hemisphere: the role of stationary Rossby waves *J. Clim.* **24** 4773–92

Screen J A and Simmonds I 2014 Amplified mid-latitude planetary waves favorer particular regional weather extremes *Nat. Clim. Change* **4** 704–9

Seo K-H and Lee H-J 2017 Mechanisms for a PNA-like teleconnection pattern in response to the MJO *J. Atmos. Sci.* **74** 1767–81

Seo K-H, Lee H-J and Frierson D M W 2016 Unraveling the teleconnection mechanisms that induce wintertime temperature anomalies over the Northern hemisphere continents in response to the MJO *J. Atmos. Sci.* **73** 3557–71

Seo K-H and Son S-W 2012 The global atmospheric circulation response to tropical diabatic heating associated with the Madden–Julian oscillation during northern winter *J. Atmos. Sci.* **69** 79–96

Simpson I R, Seager R, Ting M and Shaw T A 2016 Causes of change in Northern hemisphere winter meridional winds and regional hydroclimate *Nat. Clim. Change* **6** 65–70

Sobolowski S, Gong G and Ting M 2011 Investigating the linear and nonlinear stationary wave response to anomalous North American snow cover *J. Atmos. Sci.* **68** 904–17

Sun C, Li J, Feng J and Xie F 2015 A decadal-scale teleconnection between the North Atlantic oscillation and subtropical eastern Australian rainfall *J. Clim.* **28** 1074–92

Takaya K and Nakamura H 2001 A formulation of a phase-independent wave-activity flux for stationary and migratory quasigeostrophic eddies on a zonally varying basic flow *J. Atmos. Sci.* **58** 608–27

Teng H and Branstator G 2019 Amplification of waveguide teleconnections in the boreal summer *Curr. Clim. Change Rep.* **5** 421–32

Teng H, Branstator G, Tawfik A B and Callaghan P 2019 Circumglobal response to prescribed soil moisture over North America *J. Clim.* **32** 4525–45

Teng H, Branstator G, Wang H, Meehl G A and Washington W M 2013 Probability of US heat waves affected by a subseasonal planetary wave pattern *Nat. Geosci.* **6** 1056–61

Ting M, Wang H and Yu L 2001 Nonlinear stationary wave maintenance and seasonal cycle in the GFDL R30 GCM *J. Atmos. Sci.* **58** 2331–54

Ting M and Yu L 1998 Steady response to tropical heating in wavy linear and nonlinear baroclinic models *J. Atmos. Sci.* **55** 3565–82

UNDRR, CRED 2020 *Human Cost of Disasters: An Overview of the Last 20 Years 2000–2019* (UN Office of Disaster Risk Reduction (UNDRR))

Wallace J M and Gutzler D S 1981 Teleconnections in the geopotential height field during the Northern Hemisphere winter *Mon. Weather Rev.* **109** 784–812

Wirth V 2020 Waveguidability of idealized midlatitude jets and the limitations of ray tracing theory *Weather Clim. Dyn.* **1** 111–25

Woollings T, Li C, Drouard M, Dunn-Sigouin E, Elmestekawy K A, Hell M and Spengler T 2023 The role of Rossby waves in polar weather and climate *Weather Clim. Dyn.* **4** 61–80

Wu B and Francis J A 2019 Summer Arctic cold anomaly dynamically linked to East Asian heat waves *J. Clim.* **32** 1137–50

Wu Z, Wang B, Li J and Jin F 2009 An empirical seasonal prediction model of the east Asian summer monsoon using ENSO and NAO J. Geophys. Res. **114**

Xie S and Kosaka Y 2016 Interannual variability and predictability of summer climate over the Northwest Pacific and East Asia *Dynamics and Predictability of Large-Scale, High-Impact Weather and Climate Events* (Cambridge University Press) pp 333–42

Xu P, Wang L and Chen W 2019 The British-Baikal corridor: a teleconnection pattern along the summertime polar front jet over Eurasia *J. Clim.* **32** 877–96

Xu P, Wang L, Chen W, Chen G and Kang I S 2020 Intraseasonal variations of the British–Baikal corridor pattern *J. Clim.* **33** 2183–200

Xu P, Wang L, Dong Z, Li Y, Shen X and Chen W 2022 The British–Okhotsk corridor pattern and its linkage to the silk road pattern *J. Clim.* **35** 5787–804

Xu P, Wang L, Vallis G K, Geen R, Screen J A, Wu P and Chen W 2021 Amplified waveguide teleconnections along the polar front jet favor summer temperature extremes over northern Eurasia *Geophys. Res. Lett.* **48** e2021GL093735

Zhu Z and Li T 2016 A new paradigm for continental US summer rainfall variability: Asia–North America teleconnection *J. Clim.* **29** 7313–27